



RESEARCH ARTICLE

10.1029/2017EA000351

Key Points:

- The M_w 5.7 Ocotillo aftershock of the El Mayor-Cucapah earthquake extended north from a mainshock surface fracture to the Elsinore fault
- Postseismic slip on the Yuha fault and Ocotillo section and uplift in the Salton Trough continued for several years following the event
- Salton Trough spreading causes left slip on the Yuha fault resulting in a left step that links the Laguna Salada and Elsinore faults

Correspondence to:

A. Donnellan,
andrea@jpl.caltech.edu

Citation:

Donnellan, A., Parker, J., Heflin, M., Lyzenga, G., Moore, A., Ludwig, L. G., et al. (2018). Fracture advancing step tectonics observed in the Yuha Desert and Ocotillo, CA, following the 2010 M_w 7.2 El Mayor-Cucapah earthquake. *Earth and Space Science*, 5. <https://doi.org/10.1029/2017EA000351>

Received 22 NOV 2017

Accepted 2 AUG 2018

Accepted article online 14 AUG 2018

©2018. The Authors.

This is an open access article under the terms of the Creative Commons Attribution-NonCommercial-NoDerivs License, which permits use and distribution in any medium, provided the original work is properly cited, the use is non-commercial and no modifications or adaptations are made.

Fracture Advancing Step Tectonics Observed in the Yuha Desert and Ocotillo, CA, Following the 2010 M_w 7.2 El Mayor-Cucapah Earthquake

Andrea Donnellan¹ , Jay Parker¹ , Michael Heflin¹ , Gregory Lyzenga¹ , Angelyn Moore¹ , Lisa Grant Ludwig² , John Rundle³ , Jun Wang⁴ , and Marlon Pierce⁴ 

¹Jet Propulsion Laboratory, California Institute of Technology, Pasadena, CA, USA, ²Program in Public Health, University of California, Irvine, CA, USA, ³Physics and Earth & Planetary Science, University of California, Davis, CA, USA, ⁴Pervasive Technology Institute, Indiana University Bloomington, Bloomington, IN, USA

Abstract Uninhabited aerial vehicle synthetic aperture radar (UAVSAR) observations 2009–2017 of the Yuha Desert area and Global Positioning System (GPS) time series encompassing the region reveal a northward migrating pattern of deformation following the 4 April 2010 M_w 7.2 El Mayor-Cucapah (EMC) earthquake. The north end of the EMC rupture exhibits an asymmetric pattern of deformation that is substantial and smooth northeast of the rupture and limited but with surface fracturing slip northwest. The earthquake triggered ~1 cm of surface coseismic slip at the Yuha fault, which continued to slip postseismically. 2.5 cm of Yuha fault slip occurred by the time of the 15 June 2010 M_w 5.7 Ocotillo aftershock and 5 cm of slip occurred by 2017 following a logarithmic afterslip decay 16-day timescale. The Ocotillo aftershock triggered 1.4 cm of slip on a northwest trend extending to the Elsinore fault and by 7 years after the EMC earthquake 2.4 cm of slip had accumulated with a distribution following an afterslip function with a 16-day timescale consistent with other earthquakes and a rate strengthening upper crustal sedimentary layer. GPS data show broad coseismic uplift of the Salton Trough and delayed postseismic motion that may be indicative of fluid migration there and subsidence west of the rupture extension, which continues following the earthquake. The data indicate that the Elsinore, Laguna Salada, and EMC ruptures are part of the same fault system. The results also suggest that north-south shortening and east-west extension across the region drove fracture advancing step tectonics north of the EMC earthquake rupture.

Plain Language Summary Airborne radar and Global Positioning System observations of the Yuha Desert and Salton Trough suggest that the 2010 M_w 7.2 El Mayor - Cucapah earthquake rupture, the Laguna Salada fault in Baja California, Mexico, and the Elsinore fault in California are part of the same fault system. The M_w 5.7 Ocotillo aftershock links these faults and is a result of stress propagation from afterslip on the El Mayor - Cucapah rupture. Further east in the Salton Trough fluid migration also contributes to the observed results.

1. Introduction

The M_w 7.2 El Mayor-Cucapah (EMC) earthquake occurred 4 April 2010 in Baja California, Mexico (Hauksson et al., 2011). The fault ruptured northward to southernmost California just across the California/Mexico border (Figure 1). Two main fault segments connected by a smaller extensional fault ruptured away from the epicenter with dominantly right-lateral strike-slip motion (J. M. Fletcher et al., 2014; Huang et al., 2017; Kyriakopoulos et al., 2017; Wei et al., 2011) and with an additional smaller segment striking slightly more northerly terminating the north end of the rupture. The segments dip northwest south of the epicenter and northeast north of the epicenter. At the north end of the rupture 10–30 cm of slip also occurred on the west dipping Laguna Salada fault (J. M. Fletcher et al., 2014). The earthquake triggered slip on numerous faults in the Yuha Desert and Salton Trough to the northeast of the rupture up to and including slip on the Southern San Andreas fault (Donnellan et al., 2014; Rymer et al., 2011; Treiman, 2012). Slip in the Yuha Desert occurred on a network of orthogonal fault segments typically about 3–5 km long extending about 6 km north of the United States-Mexican border and 9 km southeast of the community of Ocotillo. These fault segments remain distinct structures at depth and are seismically active individually for a few days to weeks with seismicity migrating along adjacent fault segments (Kroll et al., 2013). EMC postseismic deformation can be explained by fault afterslip with a short timescale on the order of 10 days and fluid diffusion from an

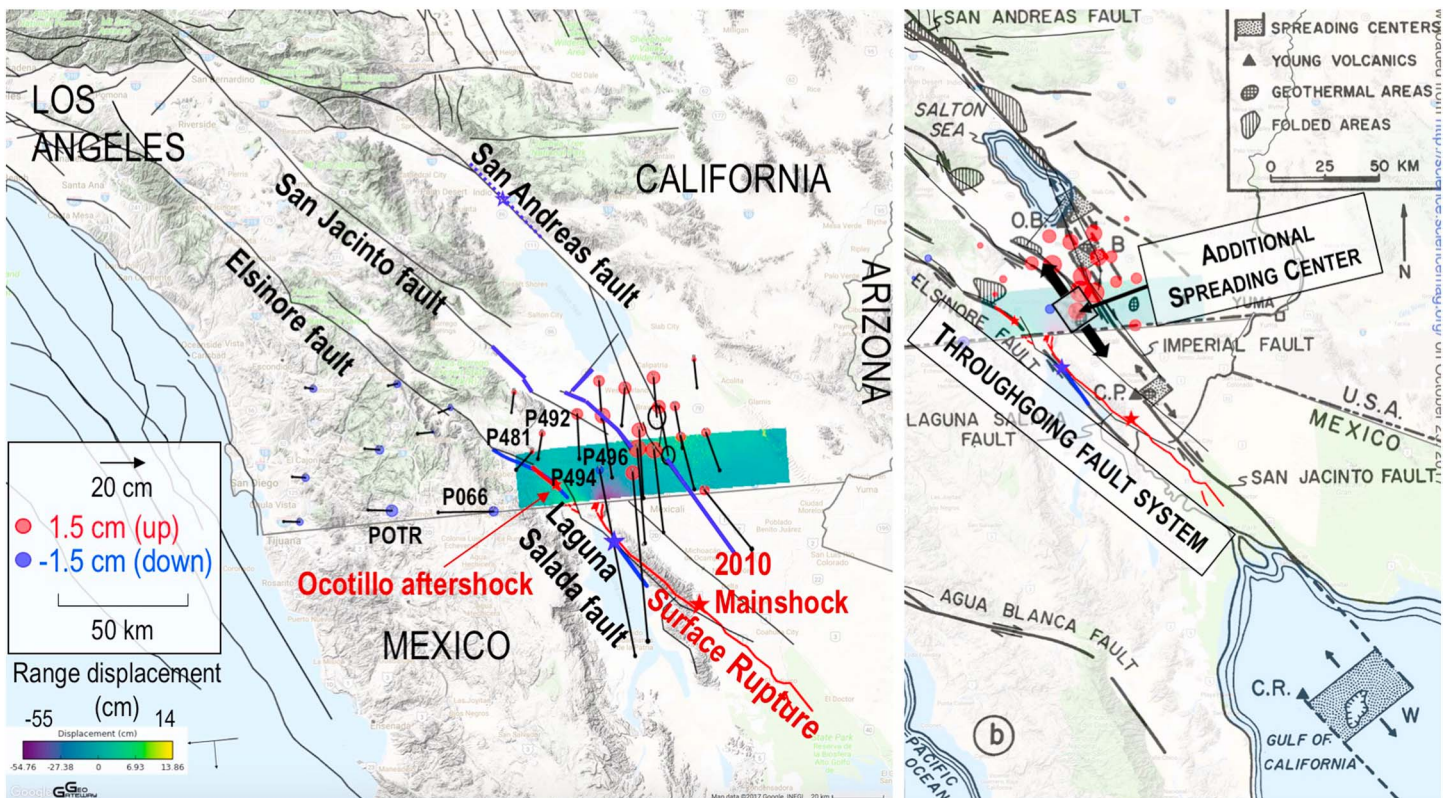


Figure 1. Study location. Left: The $M_w7.2$ El Mayor-Cucapah mainshock and the $M_w5.7$ Ocotillo aftershock epicenters shown at red stars. The surface rupture up to the Mexico/California border is shown in red. Ocotillo aftershock section identified in this study is shown as a red line. The Elders et al. (1972) mapped Ocotillo section connecting the Laguna Salada and Elsinore faults is shown underneath. The 1892 Laguna Salada earthquake and approximate rupture are shown by blue star and line along with other past ruptures discussed in the text. State boundaries are outlined in gray. Faults are black with the major faults labeled. Global Positioning System coseismic displacement vectors are shown as black vectors with error ellipses, and vertical displacements by red (uplift) or blue (subsidence) circles. Stations shown in Figure 6 are labeled. The 26501 uninhabited aerial vehicle synthetic aperture radar interferogram that includes a pair of images collected 21 October 2009 and 13 April 2010 is shown as the swath ranging from light green (displacement northwest) to purple (displacement southeast). The aircraft was flying to the west and looking south. Purple denotes motion away from the airborne instrument and yellow toward the instrument. Right: Similar plot but shown with Figure 7 from Elders et al. (1972; reprinted with permission from American Association for the Advancement of Science) superimposed. Additional spreading center identified in this study is noted.

origin just north of the main surface rupture based on seismicity and Global Positioning System (GPS) data (Ross et al., 2017). The east section of the Laguna Salada fault became active ~35 days after the EMC event (Kroll et al., 2013). In this paper we address how the gap between the Laguna Salada and Elsinore faults is connected and better define where the crust is affected by simple afterslip and stress propagation or with additional possible fluid migration.

On 15 June 2010, 71 days after the mainshock, a $M_w5.7$ aftershock occurred 9 km southeast of the community of Ocotillo at the northern end of the EMC rupture and aftershock zone (Hauksson et al., 2011; Kroll et al., 2013, 2017; Ross et al., 2017). The aftershock sequence extended 6 km northwestward from the epicenter of the Ocotillo aftershock (Kroll et al., 2017). The main Ocotillo aftershock sequence continued for about 20 days following the event (Kroll et al., 2017).

1.1. Geologic Setting

The pattern of deformation associated with the Ocotillo aftershock is consistent with the broader tectonic deformation within the Salton Trough. Elders et al. (1972) describe the Salton Trough as the landward extension of the Gulf of California spreading center, which is dilating as right-lateral shear separates the Pacific and North American plates. Extensional and transform tectonic regimes are manifest in the Imperial Valley and Salton Trough by high heat flow, Quaternary volcanism, and hydrothermal activity associated with magma intrusion at shallow depth (Hill et al., 1990; Irwin, 1990) as well as abundant seismicity along northwest

trending right-lateral strike-slip faults and northeast trending left-lateral conjugate faults, and shallow swarms of earthquakes (Irwin, 1990; Nicholson et al., 1986). The crust thins as tensional zones form between the Cerro Prieto, Imperial, and San Andreas faults over a mantle upwelling. A broad pattern of uplift occurred in the Salton Trough associated with the EMC earthquake (Figure 1), consistent with the presence of a mantle upwelling. The geodetic imaging data and high heat flow provide evidence that a spreading center is present between the northern Cerro Prieto fault and southern Superstition Hills fault in addition to those identified by Elders et al. (1972).

Paleoseismic and historic records show that the Salton Trough is capable of producing large earthquakes in the transition zone between the extensional and transform regimes, such as the southern San Andreas fault rupture in ~1700 CE (Sieh & Williams, 1990; Working Group on California Earthquake Probabilities (WGCEP), 2008), and the 1892 Laguna Salada earthquake, which Hough and Elliot (2004) describe as one of the largest earthquakes in California and Baja California in historic times (Figure 1). Other important historic earthquakes include the 1940 M_w 7.0 El Centro and 1979 M_w 6.5 Imperial Valley earthquakes, which ruptured overlapping sections of the Imperial fault (Toppozada et al., 2002) and conjugate pairs of ruptures such as the 1968 M_w 6.6 Borrego Mountain earthquake that triggered slip on the Superstition Hills fault (Nicholson et al., 1986). In 1987, the M_w 6.2 Elmore Ranch earthquake occurred on the northeast trending Elmore Ranch fault and triggered M_w 6.6 earthquake on the conjugate northwest trending Superstition Hills fault, in the southernmost San Jacinto fault zone (Hill et al., 1990; Hudnut et al., 1989). The southern Elsinore fault zone has not ruptured historically.

The southern Elsinore fault is slipping at a long-term rate of approximately 1–2 mm/year, which is slower than the northern Elsinore fault (Dorsey et al., 2012), suggesting that some deformation might be transferring to conjugate cross faults in the region. The paleoseismic slip estimate for the northern Elsinore fault is 4–5 mm/year (Magistrale & Rockwell, 1996; Millman & Rockwell, 1986; Rockwell et al., 1990; Vaughan & Rockwell, 1986). As currently mapped, the southern Coyote Mountains segment of the Elsinore fault zone is separated from the northern Laguna Salada fault zone, which ruptured in 1892, by a releasing stepover with several northeast trending cross faults (Isaac, 1987). Slip rate on the Laguna Salada fault is 2–3 mm/year (Mueller & Rockwell, 1995). Of note, Elders et al. (1972) show an Elsinore fault that extends to the Mexican border and that, in effect, continues as the Laguna Salada fault in Mexico. Isaac (1987) defined the area between the two faults, separated by a left step, as a seismic gap. Total slip from the Ocotillo aftershock and postseismic motion correlated with Elders et al. (1972) southernmost mapped section of the Elsinore fault, suggesting that these two fault systems are part of one fault system.

2. Methods

For this study we combined uninhabited aerial vehicle synthetic aperture radar (UAVSAR) and Global Positioning System (GPS) measurement of crustal deformation encompassing the Yuha Desert to characterize fault slip and broader deformation. We used GeoGateway (<http://geo-gateway.org>) to carry out the analysis. GeoGateway is a web-based science gateway that allows analysis of UAVSAR interferometric synthetic aperture radar (InSAR) data to be analyzed in the context of other geophysical, geologic, and geodetic data sources. Such sources include seismicity from the U.S. Geological Survey (USGS) catalog, fault data from Uniform California earthquake rupture forecast (Field et al., 2013), and GPS position time series (Zumberge et al., 1997). We estimated coseismic and postseismic fault slip on the Yuha fault and what we refer to as the Ocotillo section of the Elsinore fault, different from the Ocotillo section identified as a northeasterly seismic trend by Treiman (2012) that crosses the Ocotillo section discussed here.

2.1. UAVSAR

UAVSAR is National Aeronautics and Space Administration's airborne L-band InSAR platform. InSAR measurements provide line-of-sight changes at an oblique angle from a point on the ground to the instrument for pairs of images. UAVSAR flies on a Gulfstream-III aircraft at 12.5-km altitude. The instrument looks left, covering an elevation angle from about 27° to 67°, which results in a 15-km-wide swath that is typically about 90 km long. The phase of the reflected radar signal at the airborne instrument is recorded. Repeated flight path images are compared, and any ground motion between observation epochs results in a phase offset. The UAVSAR product is an array of line-of-sight ground range changes in phase that correspond to distance offsets. A radar pixel in an unwrapped image has a surface extent of ~7 m, providing correspondingly high-resolution images of ground deformation.

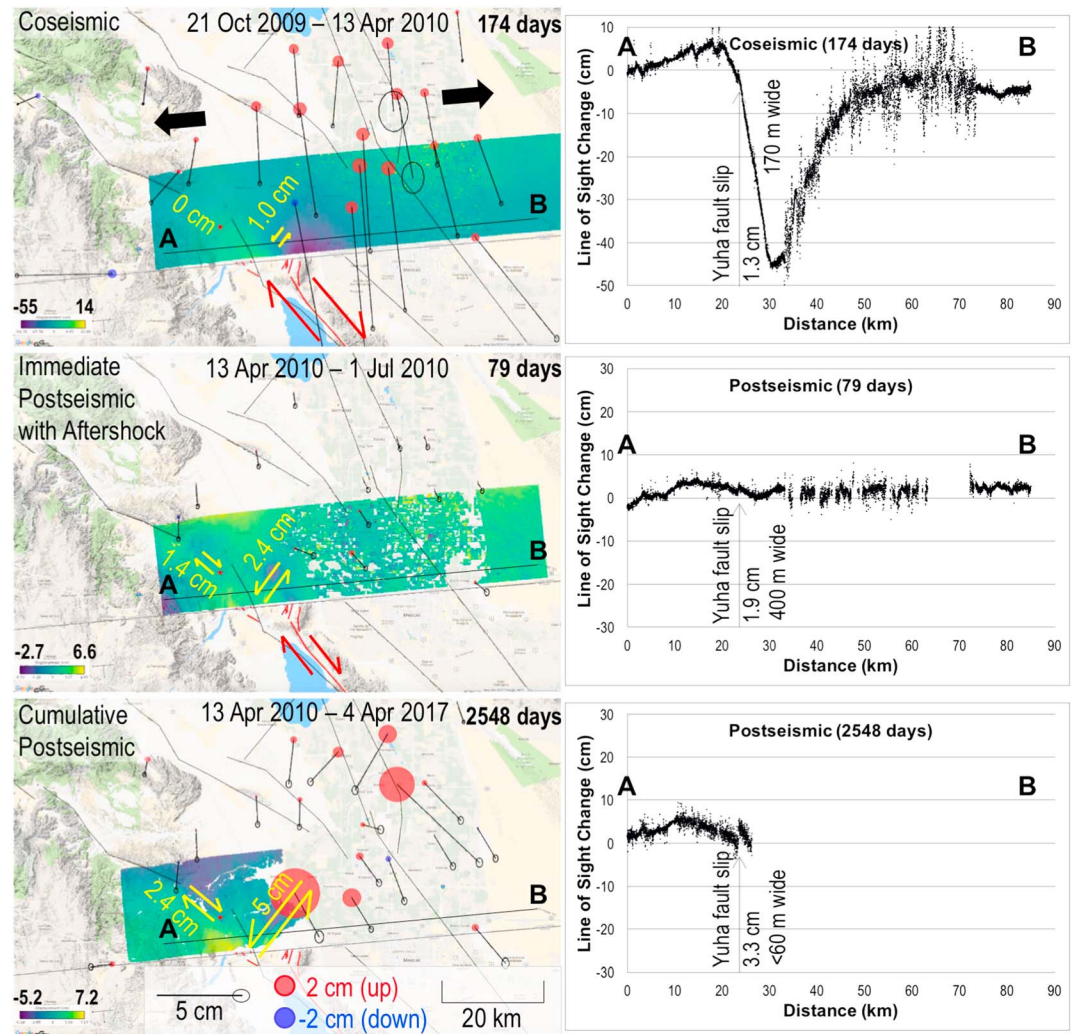


Figure 2. UAVSAR products for a 174-day pair spanning the El Mayor-Cucapah earthquake (top left), a 79-day pair from 1 week after the earthquake and spanning the Ocotillo aftershock (middle left), and 7-year total cumulative postseismic motion starting 1 week after the mainshock (bottom left). GPS vectors for the time frame corresponding to the image pair are shown in black with error ellipses. Red and blue circles show uplift and subsidence as red or blue circles. Right plots show the line-of-sight change for the profile A-B marked on the map. Red and yellow vectors illustrate where the slip occurs in each time frame.

UAVSAR became operational in 2009, 6 months before the April 2010 M_w 7.2 EMC earthquake. At the time, the observations extended south to the Mexican border in nearly east-west swaths. The earthquake rupture extended northward just past the United States-Mexico border, making it possible to study northward effects from the earthquake such as triggered slip (Donnellan et al., 2014; Rymer et al., 2011) and coseismic deformation and postseismic motion for the EMC earthquake and the Ocotillo aftershock (this study).

We here examine swath SanAnd_26501 (Figure 1) that was flown approximately every 6–12 months since UAVSAR became operational with repeats planned into 2019. Data were collected about 1 week after the April 2010 EMC earthquake, about 2 weeks after the 15 June 2010 M_w 5.7 Ocotillo aftershock, and in September and December 2010. For this line 26501 the airplane flies west at a heading of 265° and looks left, so the results provide deformation to/from the direction of the aircraft at elevation angles ranging from 27° to 67° . There is not an opposite looking swath due to the political boundary and lack of authorization to fly UAVSAR over Mexico at that time.

InSAR crustal deformation results, such as from UAVSAR, are typically represented in the form of fringe maps with each color cycle corresponding to a phase cycle of the radar wavelength. UAVSAR data are distributed as prerendered high-resolution images with InSAR fringe patterns. The mapping between pixel color and pixel value is not a one-to-one mapping from the InSAR fringe phase offset and presents interpretation challenges, particularly due to ambiguity in the trend of the color cycles relative to the sign of the observed range change. In general, we find the observations to be more easily interpretable by using a single color range to represent the full range of values of motion to/from the instrument, rather than wrapping cycles of repeating color (Figures 1 and 2). The GeoGateway interface allows users to display the original images or to convert to a color range. The color is user tunable, and users can stretch the color map for the displayed color or specify the color range. We developed a histogram-based, nonlinear color template generation algorithm to generate color maps that directly reflect the pixel values of displacement as an addition to the prerendered images (Wang et al., 2015). A web service implemented through the GeoGateway interface enables on-the-fly coloring of UAVSAR images for users to define the range of displacement and color scheme. Our default color scheme also provides a more accessible shading palette for color-vision impaired users.

We plotted the UAVSAR results for three time frames associated with the EMC earthquake (Figure 2). The coseismic time frame spans from 6 months before the earthquake to 1 week after the earthquake. The second time frame spans from 1 week after the mainshock to 2 weeks after the Ocotillo aftershock. The last time frame shows the cumulative postseismic motion from 1 week after the earthquake to 7 years after the event. Line-of-sight profiles extracted from the three lines show that the bulk of the coseismic deformation in the image occurred northeast of the rupture. Far less surface deformation occurred to the northeast of the rupture, but clear discontinuities from surface fractures are apparent. The profile A-B in Figure 2 crosses the Yuha fault, which is noted on the line-of-sight plots, showing how slip on that fracture increases over time.

2.2. GPS

GPS measurements provide north, east, and up motions of stations, complementing the UAVSAR measurements and enabling a better assessment of the three-dimensional deformation field. GPS solutions for this paper were generated with the GIPSY-OASIS II software package in Precise Point Positioning mode (Zumberge et al., 1997), with final precise orbits reprocessed in the IGB08 reference frame (Desai et al., 2011). We downloaded the products for continuous GPS stations in the Salton Trough area from <http://sideshow.jpl.nasa.gov/post/series.html>. The continuous GPS stations are part of the Plate Boundary Observatory, and daily solutions are produced from data sampled every 5 min over a 24-hr period. Results are automatically updated every week. We used time series (Jet Propulsion Laboratory, 2018) that have been postprocessed with GipsyX (Bar-Sever, 2016) software tools to detect breaks, remove outliers, and perform a fit for each site. Fit parameters include a position, a velocity, breaks in the time series, and annual and semiannual terms.

GeoGateway (<http://geo-gateway.org/main.html>) software tools were used to compute interseismic, coseismic (Figure 1), postseismic (Figure 2), and total displacements based on GPS time series and fit parameters from the Jet Propulsion Laboratory. Each site has a single long-term velocity estimate. Nonlinear motion is accommodated by breaks and seasonal terms. Interseismic displacements were estimated using the long-term velocity estimate for each site. Coseismic displacements were estimated by integrating breaks in a narrow time window around an event. Postseismic displacements were estimated by integrating breaks in a wider time window following an event. Total displacements between two times were computed directly from the time series. GeoGateway software tools download information from Jet Propulsion Laboratory and then compute east, north, and vertical displacements with error bars for all GPS sites inside a user specified time window and region of interest and can be relative to a specified site.

Here we utilized the postseismic option from the GeoGateway GPS analysis tools and integrated the breaks from the long-term trend (Figure 2). This removes the long-term tectonic motion, and long-term vertical trends that may be due to inflation or subsidence. The method allows for the results to be independent of a reference station, which could otherwise propagate its local movements or instabilities into the network results. The GPS results were necessary to understand the broader coseismic and postseismic motions from the EMC earthquake.

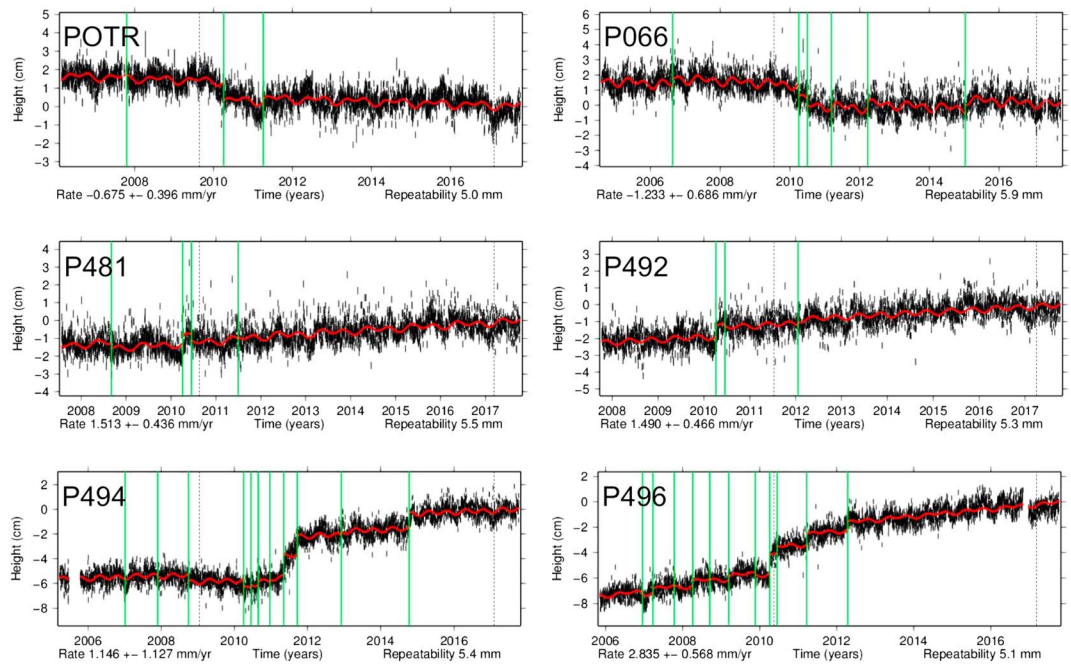


Figure 3. GPS vertical time series for stations west and east of the rupture (top and bottom) and north of the extension of the El Mayor-Cucapah rupture (middle). Stations are noted in Figure 1. Time of first and last uninhabited aerial vehicle synthetic aperture radar observations are marked by vertical dashed lines. Vertical green lines mark locations of breaks detected in the time series.

We plotted the long-term vertical time series for GPS stations surrounding the north end of the EMC rupture (Figure 3). The results show that stations to the west of the rupture extension moved downward for about 1 year associated with the EMC earthquake. Although a break with downward motion was detected at the time of the earthquake it is possible that the downward trend started prior to the event. Two stations along

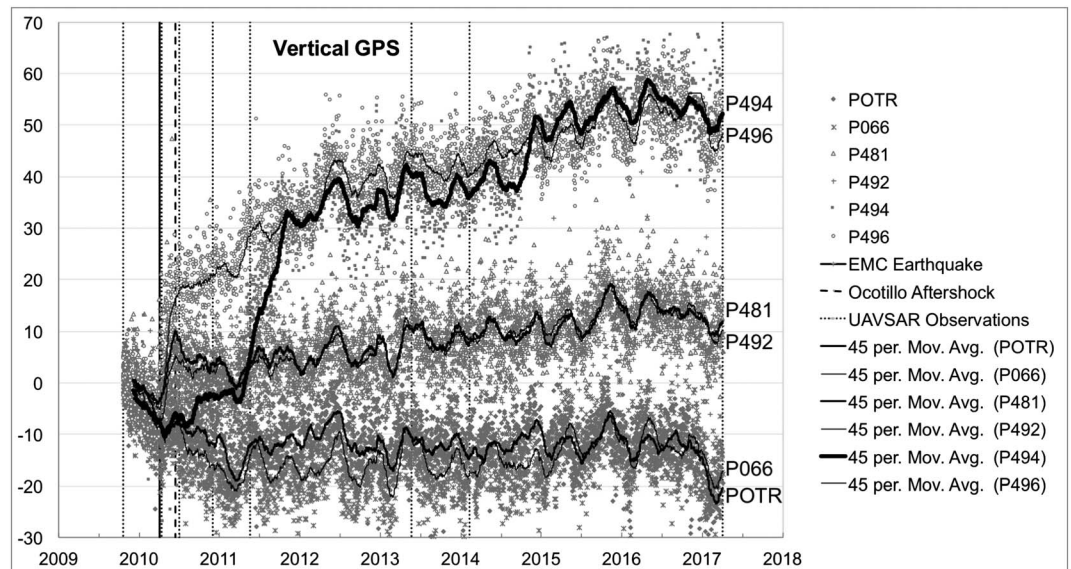


Figure 4. GPS vertical time series for the stations marked on Figure 1. A 45-day moving average trendline is plotted to show the general trend of each time series while preserving seasonal variations. Solid vertical line marks the time of the EMC earthquake. Vertical dashed line shows the time of the Ocotillo aftershock. Dotted vertical lines show the times of UAVSAR observations. EMC = El Mayor-Cucapah; GPS = Global Positioning System; UAVSAR = uninhabited aerial vehicle synthetic aperture radar.

Table 1
Parameters for the Two Four-fault Model Inversions Based on Wei et al. (2011) and Separate Inversion for the $M_{wG}5.7$ Ocotillo Aftershock

Parameter	Fault 1	Fault 2	Fault 3	Fault 4	M5.7				
Latitude (°)	32.1576	32.3005	32.1971	32.6205	32.7234				
Longitude (°)	-115.1728	-115.3035	-115.4147	-115.6341	-115.5288 ± 0.01	-115.9488			
Strike (°)	-5	-48	132	-38 ± 0.2	-51 ± 0.3	132 ± 0.01			
Dip (°)	45	75	60	50		82 ± 0.03			
Depth (km)	14	15	14	12		4.4 ± 0.02			
Width (km)	14	15	14	12		4.6 ± 0.22			
Length (km)	33	51	60	18		8.5 ± 0.22			
Strike slip (cm)	32 ± 0.1	-15 ± 0.1	-154 ± 4	-177 ± 8	16 ± 12	-24 ± 19	-5 ± 3	0 ± 5	-321 ± 6
Dip slip (cm)	-113 ± 0.1	-85 ± 0.1	-73 ± 11	29 ± 111	103 ± 17	-31 ± 24	-61 ± 4	-97 ± 9	-5 ± 1
Sense of slip	LL N	RL N	RL N	RL T	LL T	RL N	RL N	N	RL N
Dip direction	E	E	NE	NE	SW	SW	NE	NE	SW

Note. Location of the fault is at the lower left corner and the fault dips upward at the given dip angle and strikes clockwise from the left side of the rectangular fault. Sense of slip is of the upper block relative to the lower block (LL = left lateral; RL = right lateral; N = normal; T = thrust). Downdip direction is also given. Faults correspond to those in Wei et al. (2011): Fault 1 is the connecting normal fault where the rupture initiated; Fault 2 is the northern main section of the fault; Fault 3 is the southern main section of the fault; Fault 4 is the northernmost small section that ruptured into California. Parameters without errors were held fixed in the inversion. Free parameters show solved for 1σ errors. X^2/DOF is 7.9 for the first inversion and 4.7 for the second inversion. Cells that are split show results for the first and second inversion, respectively. X^2/DOF for the M5.7 aftershock is 1.2.

the northern extension of the rupture show little motion associated with the event, while station P494 north-northeast of the rupture shows a delayed uplift and station P496 further east of P494 shows uplift at the time of the earthquake with a long-term upward trend. We also plotted the time series for the time frame of the UAVSAR observations on a single plot, highlighting the delayed uplift of station P494 (Figure 4).

2.3. Geodetic Inversions

We used the four-fault model of Wei et al. (2011) to invert the coseismic GPS results for a single average slip vector on each fault segment (Table 1 and Figure 5). The fit is quite good with a resulting goodness-of-fit figure of chi-square per degree of freedom (X^2/DOF) = 7.8. A forward model of the fault slip matches the coseismic pattern of deformation observed with UAVSAR. The northernmost segment has a best fitting value of 5.1 ± 3.2 -cm right-lateral slip and 60.8 ± 3.8 cm of normal displacement. The fit is slightly better with a X^2/DOF = 4.7 if the east position and strike are allowed to vary from the Wei et al. (2011) values. In this case the best fit of this segment translates east 10 km and the strike rotates from N37°E to N51°E. For this geometry the slip is dominantly normal with 97 ± 9 -cm normal slip and 0 ± 4 -cm left-lateral strike slip. The resulting normal fault lies at the north end of the Cerro Prieto fault with a parallel strike. This model yields a more consistent southwest dipping right-lateral normal slip for the southernmost segment of the Wei et al. (2011) model than either the Wei et al. (2011) model or our inversion using the original location and geometry of the northernmost segment of the four-fault model.

To understand the deformation north and northwest of the rupture, we selected a polygon of the UAVSAR observations around the Ocotillo aftershock area with a decimation of data to approximately 125-m spacing in the east-west axis and 200-m spacing in the north-south direction. We then inverted the data for coseismic parameters for the $M_w5.7$ aftershock (Table 1 and Figure 5). The results agree with the seismic focal mechanism for the event from the USGS event page (<https://earthquake.usgs.gov/earthquakes/event-page/ci14745580#focal-mechanism>), with about 320 mm of right-lateral slip on a plane dipping steeply to the southwest. The resulting depth of this fault ranges from 4.4 to 9 km. The geodetic moment magnitude for the aftershock is M5.7, consistent with the seismic moment.

2.4. UAVSAR Slip Estimates

We used the detailed UAVSAR images to estimate slip on the Yuha fault and Ocotillo section for times ranging from 1 week after the EMC earthquake to 2017. We automatically detected spatial discontinuities in the UAVSAR images using a Canny (1986) edge detection algorithm and by selecting line-of-sight profiles across the discontinuities (Parker et al., 2017; Figure 6). Several northwest trending fractures and the Yuha fault are highlighted on the coseismic image that spans the interval from 21 October 2009 to 13 April 2010. The Ocotillo section shows a discontinuity following the 15 June 2010 $M_w5.7$ aftershock. Slip on the Yuha fault and Ocotillo section continues into 2017. The edge detection algorithm identifies slip as discontinuities in

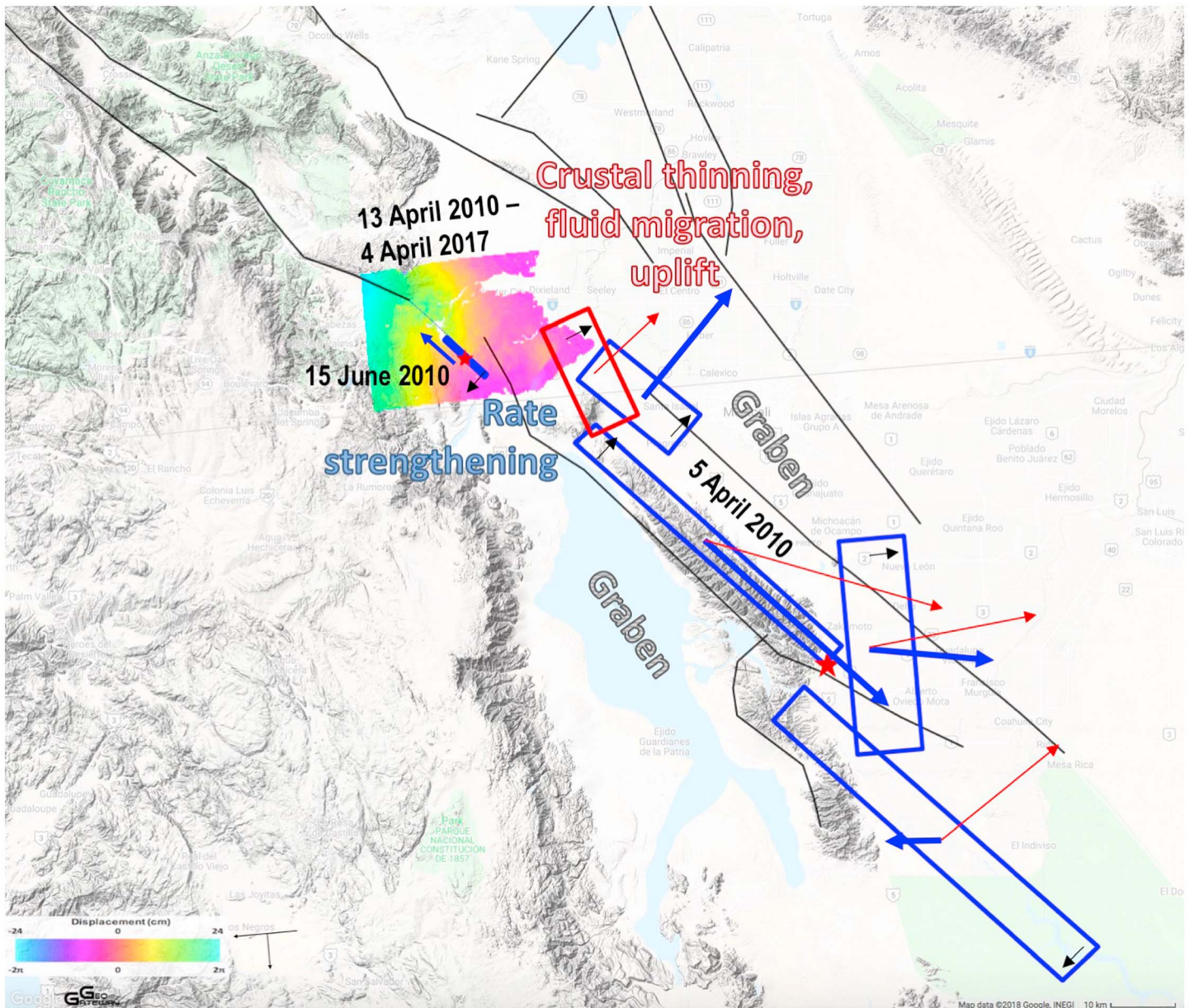


Figure 5. Regional model based on the GPS and UAVSAR observations. Blue rectangles show the best fit El Mayor-Cucapah coseismic inversion based on the Wei et al. (2011) four-fault model. Black arrows show the dip direction. Blue vectors show the displacement of the upper block in the fault model. Red rectangle shows the location of the northernmost fault in the Wei et al. (2011) model. Red vectors show the results of our inversion when the four-fault model geometry is fixed to the Wei et al. (2011) model. The fault determined from inverting the interferogram spanning the M5.7 aftershock is also shown, with displacement vector. The interferogram for the entire time span of this study shows the long-term total deformation. UCERF-3 faults are plotted in black. Tectonic interpretation is shown in outlined text.

interferometric phase that is downsampled from the full resolution ground range data to a coarser 35-m resolution grid. We plotted the fault-parallel slip estimates and fit a cubic polynomial, a function that best fits the overall slip distribution, to each time span (Figure 7). Using the peak slip for each time frame we plotted slip versus time and fit the measurements to a logarithmic afterslip decay model:

$$U = A \ln\left(\frac{t}{\tau} + 1\right) + B$$

A and B are constants and t is time (Savage and Svarc, 2009). In this model, the timescale τ represents the elapsed time for the cumulative slip to reach approximately 69% of the constant value A . The relation of this model and its parameters to physical friction laws is discussed further in the Results section below.

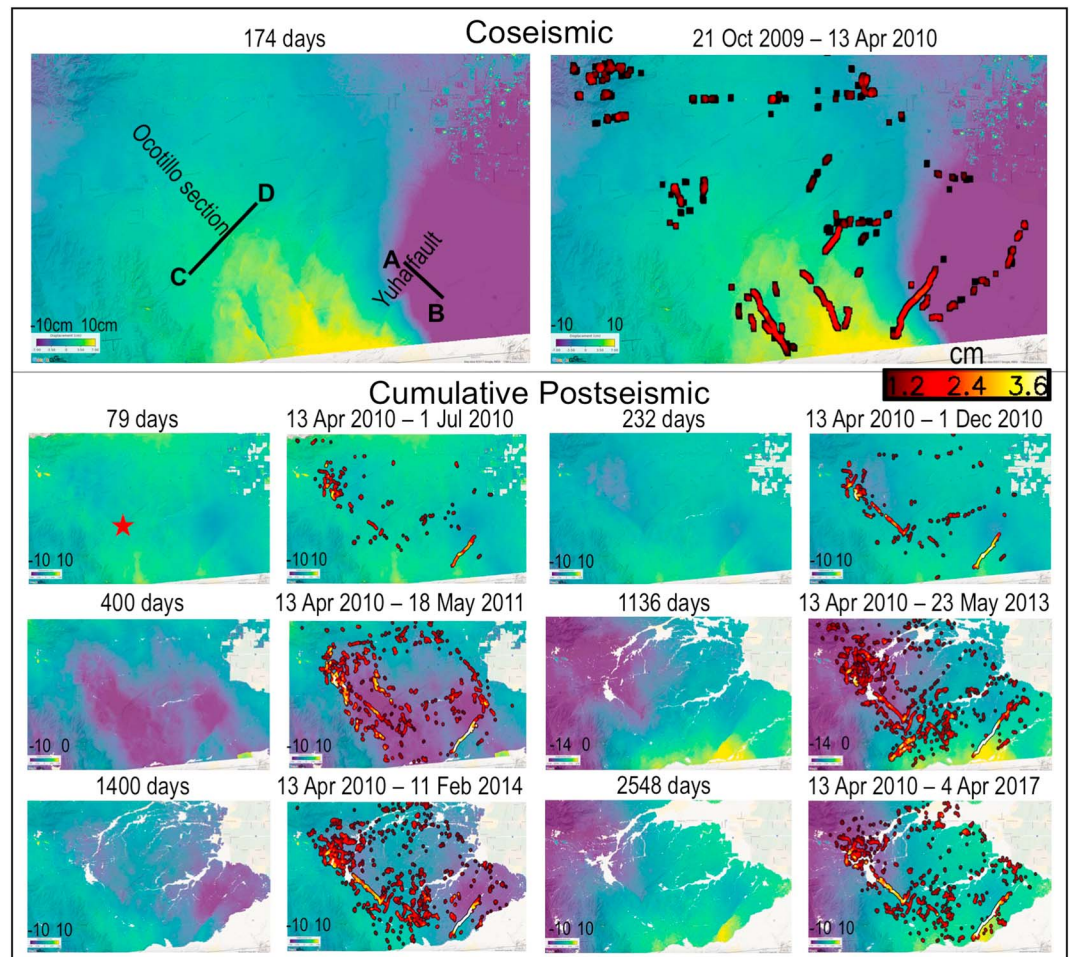


Figure 6. Interferograms spanning and following the El Mayor-Cucapah earthquake plotted with the same color range. Top left shows the coseismic interferogram. Location of the profiles for Figures 5 and 6 is shown in the top left, and the location of the Yuha fault and Ocotillo section is marked. Top right shows slip estimates at automatically identified discontinuities in the interferogram. The color scale is for slip estimates in the range direction between the ground and the airborne instrument. Bottom panels show cumulative postseismic interferograms and automated slip estimates for different time frames all starting on 13 April 2010, 1 week after the El Mayor-Cucapah earthquake.

Using the edge detection results as a guide, we selected profiles spanning the active discontinuities and examined the evolution of slip over time in across fault profiles for the Yuha fault (Figure 8) and the Ocotillo section (Figure 9). These plots display the total slip and evolution of slip over time. Fitting the afterslip logarithmic decay model described above to the data yields a robust 16-day timescale of deformation. Finally, we estimated the fault zone width from the spatial slip profiles (Figure 10). While the uncertainty in these estimates is relatively large, a picture emerges in which the Yuha fault displays narrow EMC coseismic triggered slip, subsequently broadening to ~ 300 m over the next 3 years and then narrowing again from years 4–7 to a width of 40 m. In comparison, the Ocotillo section is wider for the duration of the observations but there is a suggestion of fault zone narrowing from ~ 340 m at the time of the aftershock to ~ 250 m by 2017.

3. Results

Our results show an asymmetric pattern of EMC coseismic deformation (Figure 2) that is generally consistent with the Wei et al. (2011) four-fault model with an average uniform slip on each segment (Table 1). Both inversions fit the overall pattern of deformation, including the asymmetric pattern observed on either side of the rupture for the mainshock (Figure 2). The Wei et al. (2011) shows highly variable rake on its 3-km segments,

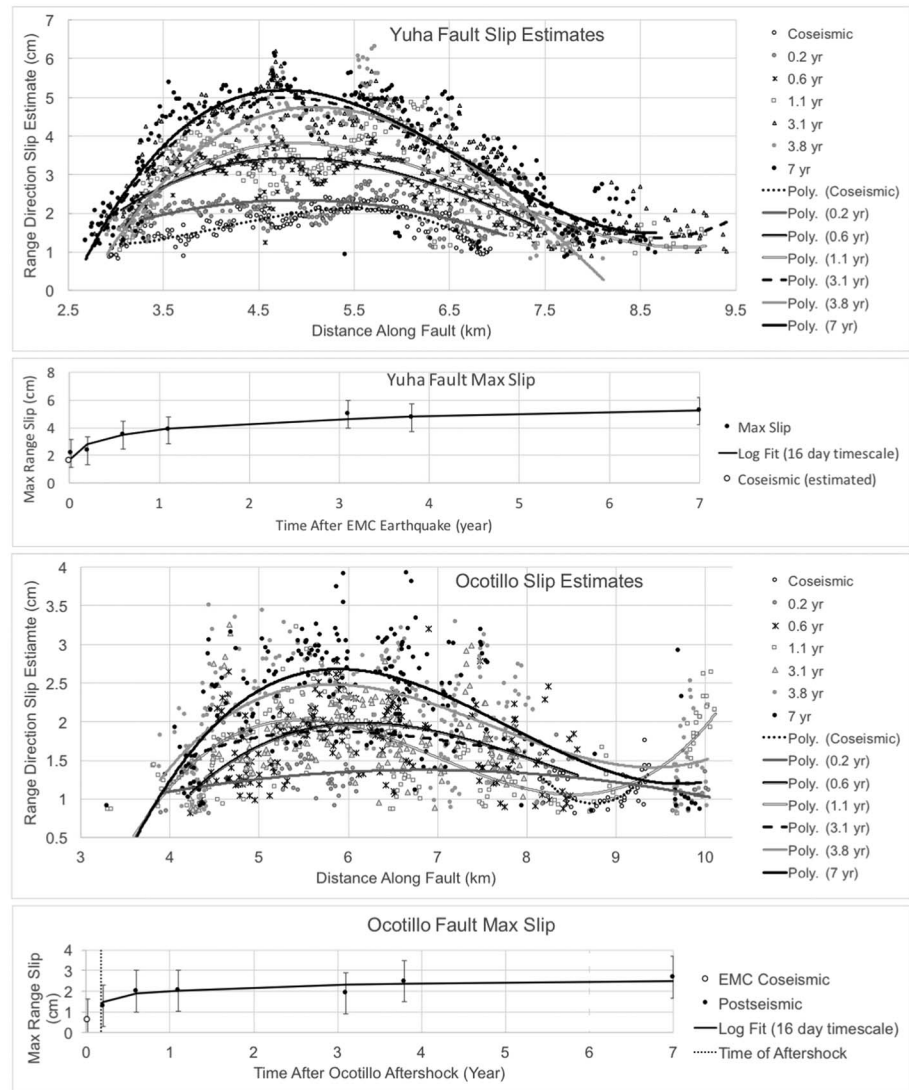


Figure 7. Fault slip estimates from the automated edge detection. A cubic polynomial is fit to each along fault slip distribution. Peak deformation at each time is plotted and a log afterslip model is fit.

and the model here, solving for average slip on each of the four-fault segments using the Wei et al. (2011) geometries, results in inconsistent right-lateral and left-lateral fault segments. Relaxing the location and strike of the northernmost segment (fault 4) results in right-lateral slip on each of the main fault segments 1–3 providing more plausible slip results. The results of the second inversion fit the data better in the Salton Trough with a normal fault dipping northeast and aligned with the Cerro Prieto fault at its north end. The results of our second model are more consistent with the sense of slip on the southernmost fault and a graben structure bounded on the east by a west dipping normal fault in the Laguna Salada basin (J. M. Fletcher & Spelz, 2009). Neither the Wei et al. (2011) model nor our coseismic inversion addresses the finer surface fracturing to the north and northwest of the EMC rupture. These inversions suggest that processes occurred at depth and in the Salton Trough that cannot be inferred from the surface rupture alone, consistent with the conclusion by Wei et al. (2011).

The Salton trough moved southward and up relative to before the earthquake from the mainshock (Figure 1). The Peninsular Ranges, west of the north end of the rupture, moved west and down relative to before the earthquake. GPS station P494, near the north end of the rupture, moved down in the mainshock (Figure 3), which is consistent with it being located on the hanging wall of the normal fault of the northernmost

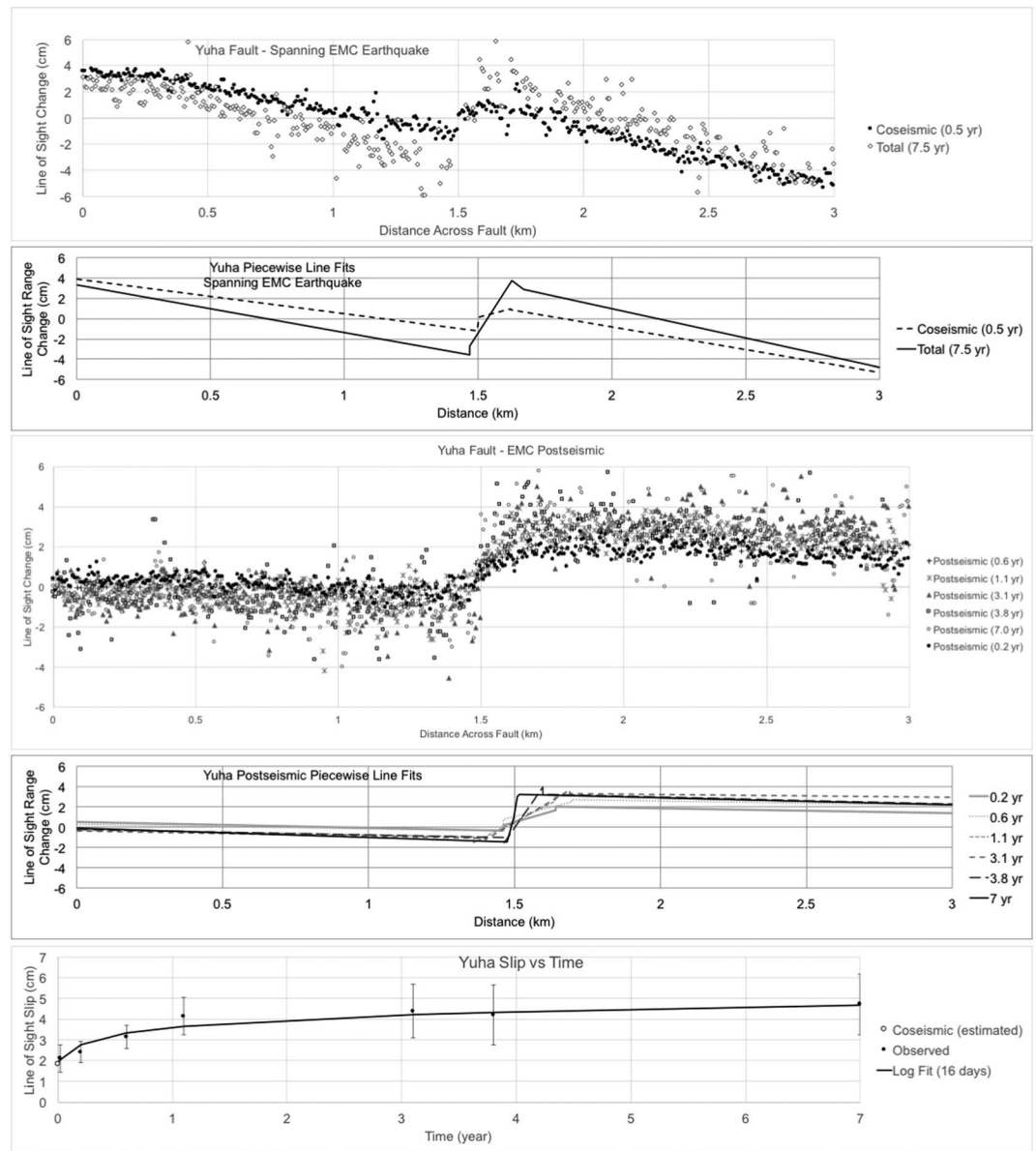


Figure 8. Yuha fault slip across profile A-B noted in Figure 4 spanning and following the El Mayor-Cucapah earthquake. Piecewise linear fits are shown under the observed data. Fault slip versus time is estimated from the line fits on either side of the fault, and a log afterslip model is fit to the data. EMC = El Mayor-Cucapah.

segment of the four-fault model. The earthquake triggered left-lateral slip at the northeast striking Yuha fault and on a network of northwest and northeast striking surface fractures in the northwest lobe of coseismic deformation up to, but not including the location of the Ocotillo aftershock and the Ocotillo fault section as defined in this paper. Seventy-one days after the EMC mainshock, the M_w 5.7 Ocotillo aftershock occurred on a northwest trending right-lateral strike-slip section. Inversion of the UAVSAR data spanning the time of the aftershock results in a fault plane of similar geometry and moment release to what can be inferred from the seismic focal mechanism. Both the Yuha fault and Ocotillo section show continued slip over 7 years that follows a rapid afterslip decay model with a 16-day timescale (Figures 6–9). This rapid decay is comparable to results for other earthquakes such as the 1966 Parkfield earthquake, the 1976 Guatemala earthquake, and the 1979 Imperial Valley earthquake (Marone et al., 1991) despite the total slip values at the surface being an order of magnitude lower than these earthquakes. The Ocotillo aftershock

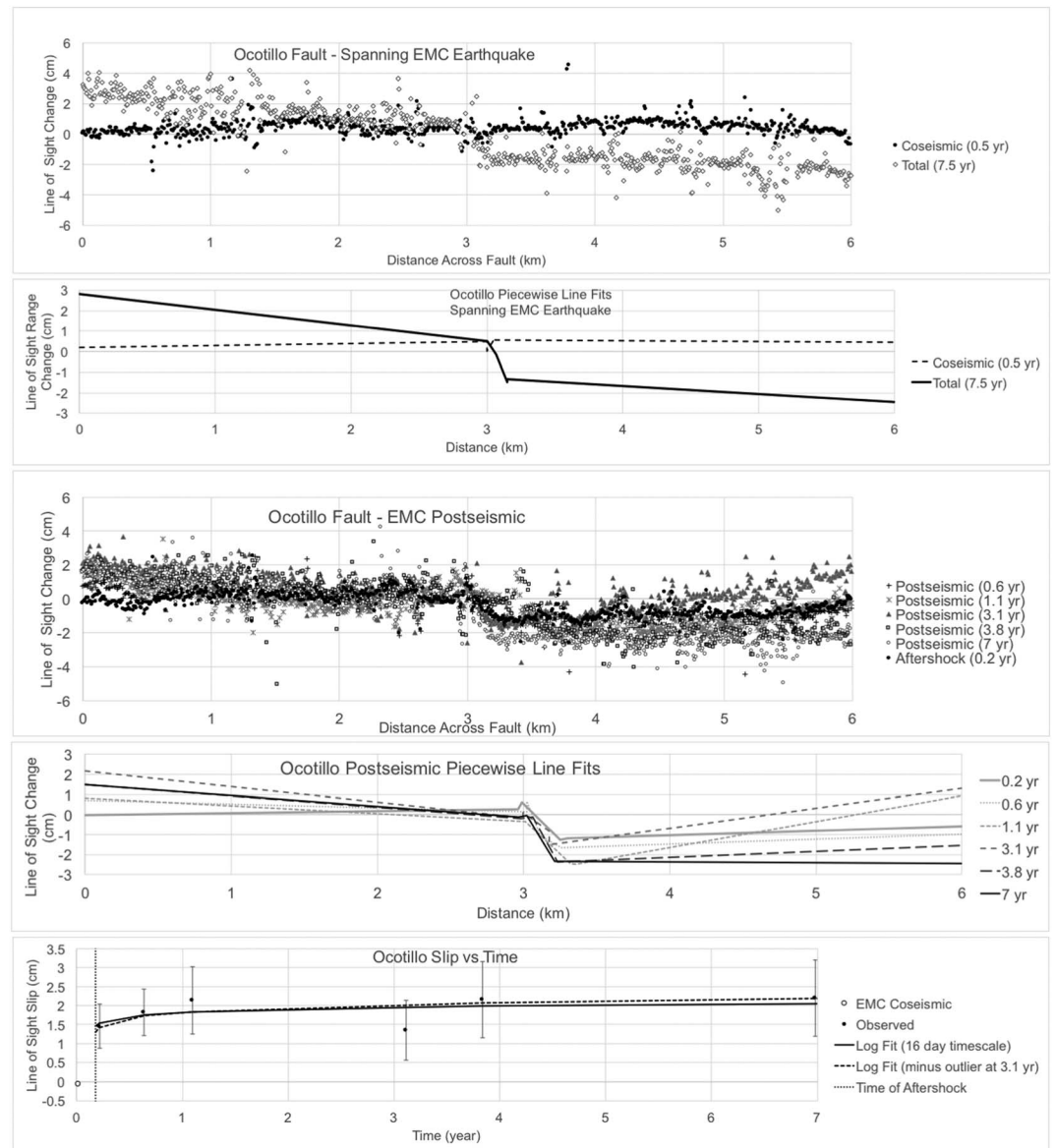


Figure 9. Ocotillo section slip across profile B-C noted in Figure 4 spanning and following the El Mayor-Cucapah earthquake. Piecewise linear fits are shown under the observed data. Fault slip versus time is estimated from the line fits on either side of the fault, and a log afterslip model is fit to the data. EMC = El Mayor-Cucapah.

and continued afterslip fits within a pattern of postseismic decay from the EMC earthquake indicating northward stress transfer following the mainshock.

The significance of this observed timescale in the afterslip decay can be appreciated by considering the rate and state friction laws that are used to explain both laboratory and field observations of transient fault behavior and afterslip (Marone et al., 1991; Scholz, 1998). Theoretical and laboratory research suggests that the time dependence of fault afterslip follows a functional form of

$$U = \frac{h\sigma_n}{G} (a - b) \ln \left[\left(\frac{GV_{cs}}{h\sigma_n(a - b)} \right) t + 1 \right]$$

In this relation, the dimensionless friction parameter $(a-b)$, or A in our above fit for afterslip, is positive in the case of velocity strengthening conditions relevant here. G is the crustal shear modulus and is the lithostatic normal stress vertically averaged over the depth h of the velocity strengthening layer. Using commonly

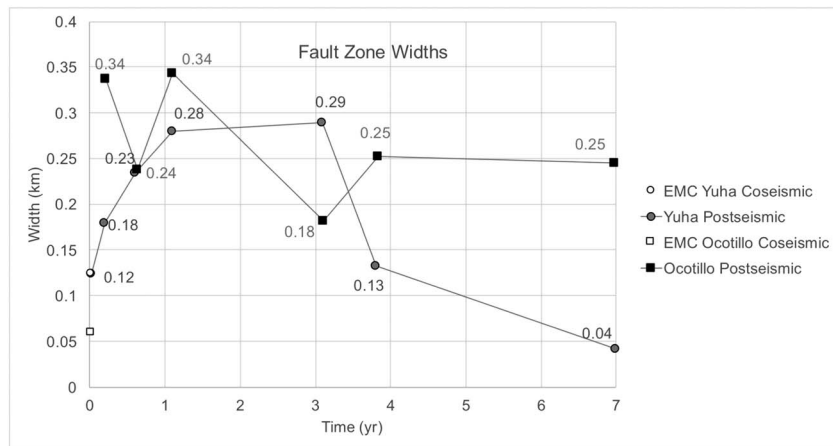


Figure 10. Fault zone widths for the Yuha fault and Ocotillo section over time. A point at 1.1 years for the Ocotillo aftershock was an outlier and removed. EMC = El Mayor-Cucapah.

accepted laboratory values for $(a-b)$ in the range 0.001–0.005 (Marone et al., 1990), our afterslip decay results projected to horizontal motion yield an estimated velocity strengthening layer thickness of ~ 2.2 km. Alternatively using the depth of the simplified aftershock inversion of 4.9 km yields an $(a-b)$ of 0.002. This result is in accord with both earlier work on fault afterslip and with our inference in this work of surface deformation mediated by a near-surface layer of unconsolidated sediments. The timescale, amplitude surface motion, and depth of the Ocotillo aftershock are consistent with rate and state friction for a rate-strengthening layer over the Ocotillo aftershock fault plane.

GPS vertical time series show a broad pattern of uplift to the east in the Salton Trough. A lesser subsidence occurred to the west of the rupture in the Peninsular Ranges into mid-2011, which could be due to warping. Station P494, located on the hanging wall of the northernmost EMC coseismic normal fault, subsides on the downdropped block in the mainshock and then shows delayed uplift that starts in early 2011 with a large jump to mid-2011 and then continued uplift into 2017 (Figure 3). The vertical time series of P494 matches the uplift of station P496 located slightly to the northeast by mid-2011, and the two stations then show nearly identical trends of uplift with annual variations into 2017 (Figure 4). These results suggest crustal spreading with migration and filling of pore fluids is occurring in the Salton Trough northeast of the origin of fluid migration identified by Ross et al. (2017).

Delineation of the Ocotillo aftershock section becomes more pronounced in the years following the event. Postseismic deformation from the aftershock is slightly greater than at the time of the aftershock producing a well-defined right-lateral zone of shear that can be identified in the UAVSAR data. The width of the Ocotillo section is about 250 m wide, which would make it difficult to locate with in situ field mapping. The section trends with a strike of 134.3° and is 19 km long. The fault zone width for both the Yuha and Ocotillo faults narrow over time suggesting healing of these faults, which should occur for a rate strengthening upper crust.

4. Discussion

A stronger lithosphere and crust in the Peninsular Ranges bounding the west side of the EMC rupture is most likely responsible for the asymmetric pattern of deformation at the north end of the mainshock (Molnar & Dayem, 2010; Pollitz et al., 2012). Our results show a northwestward propagation of postseismic deformation along this lithospheric barrier that steps left at the Yuha fault to the Ocotillo aftershock fault, which extends to the southern Elsinore fault. We term this fracture advancing step tectonics (FAST) and attribute it in part to a tectonic setting that is closer to a pure shear environment. Lab experiments show that pure shear results in a propagating pattern of fracture and slip along conjugate fault segments (Cooke, personal communication, October 9, 2017; Healy et al., 2015; Oertel, 1965). The FAST of the Yuha Desert and EMC earthquake contrasts with the simple shear environment of the North Anatolian fault in Turkey that has displayed fracture advancing tectonics as earthquakes have propagated along the fault (Stein et al., 1997; Toksöz et al., 1979). East of the lithospheric barrier in the Salton Trough fluid migration likely also contributes to ongoing deformation.

The signature of delayed and evolving shear across the conjugate Yuha fault provides further clues to the mechanics of stress and deformation in the postseismic period. The time evolution of the observed surface width of the Yuha fault starts out at 120 m at the time of the EMC earthquake, grows to 290 m over 3 years with an apparently logarithmic time dependence, and then narrows to 40 m by 7 years after the earthquake (Figure 10). Taking these width measurements as a proxy for the approximate dislocation depth, it may be possible to infer trends of vertical as well as horizontal migration in slip. The Yuha example suggests triggering of shallow surface slip in the mainshock, followed by a downward migration of slip with a pulse that then propagates to the surface. In the case of the Ocotillo section, there is no clear trend evident in the postseismic fault zone width, with the top depth of slip apparently steady at a few hundred meters. At the Ocotillo section a small amount of slip might have migrated up the fault (Figure 10). In both cases slip along the entire fault section increases with time.

In contrast to the relatively consistent width of the Ocotillo section, the left-lateral Yuha fault slip zone shows a fairly strong narrowing trend in the 3- to 7-year postseismic period. A reasonable interpretation of this result is that prompt Yuha slip at a depth of several hundred meters propagated toward the surface in the sediments east of the Ocotillo aftershock. The inference follows that the relatively unconsolidated shallow material under low confining pressure does not retain elastic strength over this time period. The ultimate fault zone width of only tens of meters is suggestive of near-surface deformation that remains confined to a narrow zone as it propagates upward. This would be in contrast to the right-lateral slip on the Ocotillo section, for which it may be inferred that the more extensively damaged near-surface layers ultimately accommodate the plastic deformation over a zone several times wider. Alternatively, this may suggest that a decrease in fault normal stress, such as by NW-SE spreading and extension, facilitated the shallow slip episode seen on the Yuha fault as suggested by the delayed and rapid uplift of GPS station P494 nearby.

Elders et al. (1972) described a series of right-lateral faults joined by spreading centers from the Gulf of California to the Salton Sea. Evidence here points to an additional spreading center at the north end of the Cerro Prieto, which could provide a connection to the Superstition Hills fault. Gravity and heat flow measurements reported in Elders et al. (1972) are consistent with the presence of this spreading center. Our four-fault coseismic slip model based on Wei et al. (2011) supports this conclusion, and our inversion fits the coseismic GPS data better with a normal fault at the northern tip of the Cerro Prieto fault, where a spreading center may be located. Initial subsidence at the north end of the EMC rupture, due to the presence of normal faulting is followed by rapid uplift that transpires over 2 years and continues for 7 years following the earthquake. This uplift is likely due to emplacement of fluids following extension. As suggested by Elders et al. (1972) and Dorsey et al. (2012) a transtensional right-lateral transform fault system extends northward from the Gulf of California and a less mature right-lateral fault system connects the Gulf of California with the western big bend of the San Andreas fault. Our results show that postseismic deformation northwest of the EMC rupture can be fit by simple fault afterslip rate and state friction, while the Salton Trough to the northeast likely has multiple processes occurring triggered by the EMC earthquake.

The Ocotillo aftershock provides the connection between the Laguna Salada and EMC fault system in Mexico, to the Elsinore fault in California. The short 8- to 13-km rupture length, embedded within an Elsinore/Laguna Salada discontinuous fault system that is over 350 km long, is consistent with evolution of an immature fault zone. The smaller M_w 5.7 Ocotillo aftershock event and the lower slip rate in this area of 1.6 mm/year compared to sections of the Elsinore fault to the north and Laguna Salada fault to the south of the aftershock raise the question of whether a larger earthquake will eventually fill in this area creating a better defined throughgoing structure. The segment drawn by Elders et al. (1972) and shown on Figure 1 is 34 km long and overlaps with the Ocotillo aftershock rupture. Perhaps, the Ocotillo aftershock initiated an incomplete rupture on this fault section. One meter of slip on the 34-km-long section would produce a M_w 6.8 earthquake. A slip rate of 1.6 mm/year results in a 625-year recurrence interval. Three meters of offset would produce a M_w 7.1 event (Hanks & Kanamori, 1979) and at a rate of 1.6 mm/year a recurrence interval of 1,875 years. Could a large earthquake that creates a throughgoing structure unlock the southern section of the Elsinore fault allowing for the slip rate to catch up either seismically or with additional postseismic slip?

There is little paleoseismic evidence for recent rupture on the southern Elsinore fault. The Temecula segment of the fault may have ruptured as recently as 185–340 years ago. This section has an average recurrence interval of 550 years, with a maximum recurrence interval of 1,100 years, and an average 2.5-m slip per event

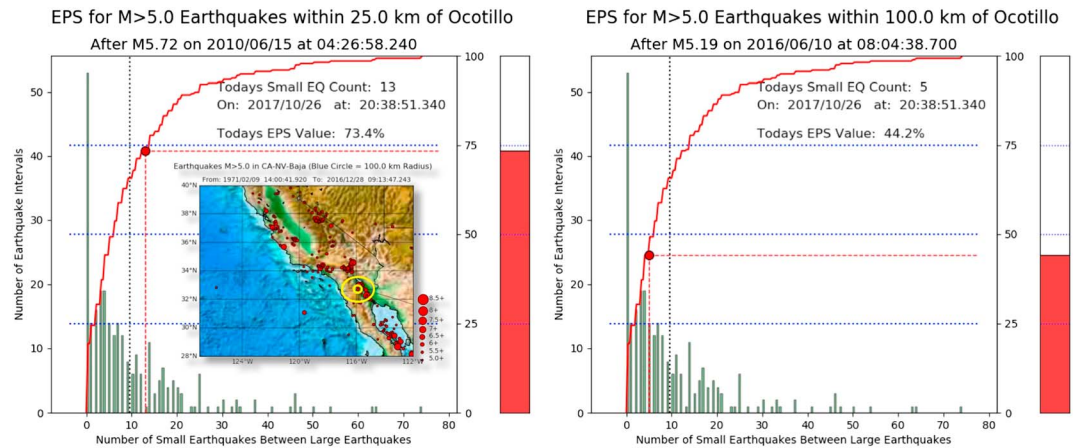


Figure 11. Nowcast for 25- and 100-km regions surrounding Ocotillo in southern California as shown in the inset map. The green vertical bars represent a histogram for the number of small earthquakes between each pair of large earthquakes. The red stair-step curve is the cumulative distribution function computed from the small earthquake histogram. Left: Nowcast for the 25-km region surrounding Ocotillo. Right: Nowcast for the 100-km region surrounding Ocotillo. Map: Large region from which statistics are drawn for the small 25- and 100-km regions shown as yellow circles. Large earthquakes are shown as red circles.

(Vaughan et al., 1999). However, it is not likely to rupture concurrently with the Julian segment adjacent and to the south, which has a recurrence interval of 3,000–3,500 years with the most recent earthquake 1,500–2,000 years ago (Thorup, 1997; Thorup et al., 1997). Overall, geodetic rate of slip for the Elsinore fault is 2.7 ± 0.6 mm/year (Meade & Hager, 2005).

K. E. Fletcher et al. (2011) find a long-term, 40,000-year, slip rate of 1.6 mm/year on the southernmost part of the Coyote Mountains segment of the Elsinore fault, just north of the Ocotillo section of the Elsinore fault identified in this study. The Elsinore fault is young, having initiated 1.2 Ma, and as a result is more complex than mature faults (Dorsey et al., 2012). The Laguna Salada fault to the south is about 97 km long and produced a M_w 7.1–7.2 earthquake in 1892, rupturing 22 km with up to 5 m of oblique dextral and normal slip (Hough & Elliot, 2004; Mueller & Rockwell, 1995). The rupture parallels the EMC rupture less than 2 km away, suggesting that the two faults are part of the same fault system. Slip rate on the Laguna Salada fault is 2–3 mm/year (Mueller & Rockwell, 1995).

To better understand the earthquake potential, we compute nowcasts for the area around the Ocotillo site within circles of radius 25 and 100 km (Figure 11). Nowcasting is a method for evaluating the current state of the fault system in a seismically active area, which is reset following a moderate to large earthquake (Rundle et al., 2016; Rundle et al., 2018). The method uses counts of small earthquakes to evaluate the potential for a large earthquake. Nowcasting is not a prediction, but it can be applied to estimate seismic risk in a region (Rundle et al., 2018). In the present calculation, which provides a snapshot of the fault system in October 2017, a small earthquake is an event having magnitude $3.99 \leq M_w < 5$, whereas a large earthquake is an event having magnitude $M_w > 5$. The statistics for the number of small earthquakes between large earthquakes are collected in the large region shown in the maps. The statistics from the large region are then applied to the small region within the blue circle. There are 274 earthquakes $M_w \geq 5.0$ in the large region since 9 February 1971 (the catalog begins at 1 January 1970). Currently, there have been 13 events $3.99 \leq M_w < 5$ earthquakes since the M_w 5.72 aftershock that occurred on 15 June 2010 within the circle of radius 25 km around the Ocotillo site using the USGS Advanced National Seismic System catalog. From this count, we determine that 73.4% of the intervals in the large region would have had five or fewer such small earthquakes between the large earthquakes. Thus, our nowcast value, or earthquake potential score (EPS), for a large earthquake in the region was 73% at time of paper submission in December 2017 and is 77% at the time of paper revision in July 2018. There have been five events $3.99 \leq M_w < 5$ earthquakes since the M_w 5.19 earthquake that occurred on 10 June 2016 within the circle of radius 100 km around the Ocotillo site. From this count, we determine that 44.2% of the intervals in the large region would have had five or fewer

such small earthquakes between the large earthquakes. Thus, our nowcast value, or EPS, for a large earthquake was 44.2% at the time of paper submission in December 2017 and 48.5% at the time of paper revision in July 2018. The EPS or nowcast value in both cases is larger for the smaller 25-km Elsinore fault area because fewer large earthquakes have occurred there than for the larger 100-km area. This raises the question whether a large earthquake on the Elsinore fault is more likely to occur now that the Ocotillo aftershock and its coseismic and postseismic slip may have unlocked a 13-km-long section at its southernmost end or whether the Ocotillo aftershock is part of the afterslip decay process for the EMC earthquake. The EPS is valid at the time it was computed; updates for future times can be found at <http://geo-gateway.org>.

5. Conclusions

The Ocotillo aftershock followed the 2010 M_w 7.2 EMC earthquake by 71 days, continuing a northward pattern of fault propagation. Left slip on the northeast striking Yuha fault facilitates a left step in the fault zone. The Ocotillo aftershock connects the Elsinore and Laguna Salada faults, creating a single 350-km-long through-going but immature fault system. The Ocotillo section of the Elsinore fault was noted in Elders et al. (1972). It is unclear why this section is not shown in subsequent fault and hazard maps (e.g., UCERF-3, Field et al., 2013). Postseismic deformation following the EMC earthquake has a typical timescale of decay and can be matched to rate and state mechanical afterslip models. These FAST processes were enabled by the transtensional plate boundary near the Salton Trough, where additional spreading centers and fluid migration is likely prevalent. A key question is whether the Ocotillo aftershock has transferred stress northward and unlocked the joining section between the Elsinore and Laguna Salada fault systems. Two large earthquakes have occurred recently to the south in 1892 and 2010. Do those earthquakes and the EMC aftershock bring the Elsinore fault closer to failure? Nowcasting using the seismic catalog suggests a high EPS for the southern Elsinore fault.

Acknowledgments

Portions of this work were carried out at the Jet Propulsion Laboratory, California Institute of Technology under contract with NASA. The work was funded by NASA's ACCESS, Geodetic Imaging, and Earth Surface and Interior programs. This material is based on data services provided by the Plate Boundary Observatory operated by UNAVCO for EarthScope (www.earthscope.org) and supported by the National Science Foundation EAR-0350028 and EAR-0732947. We thank JPL's UAVSAR team for collection and processing of the UAVSAR data. We thank Michelle Cooke for insightful discussion on fracture advancing tectonics and their stress regimes. We thank Chris Marone for rate and state discussions and particularly thank a thorough reviewer for helping us produce a much stronger paper.

References

- Bar-Sever, Y. E. (2016). December. Real-time GNSS positioning with JPL's new GIPSYx software. In AGU Fall Meeting Abstracts.
- Canny, J. (1986). A computational approach to edge detection. *IEEE Transactions on Pattern Analysis and Machine Intelligence*, 6, 679–698.
- Desai, S. D., Bertiger, W., Gross, J., Haines, B., Harvey, N., Selle, C., et al. (2011). Results from the reanalysis of global GPS data in the IGS08 Reference Frame, AGU Fall Meeting, San Francisco, CA.
- Donnellan, A., Parker, J., Hensley, S., Pierce, M., Wang, J., & Rundle, J. (2014). UAVSAR observations of triggered slip on the imperial, Superstition Hills, and East Elmore ranch faults associated with the 2010 M 7.2 El Mayor-Cucapah earthquake. *Geochemistry, Geophysics, Geosystems*, 15, 815–829. <https://doi.org/10.1002/2013GC005120>
- Dorsey, R. J., Axen, G. J., Peryam, T. C., & Kairouz, M. E. (2012). Initiation of the southern Elsinore fault at ~1.2 ma: Evidence from the fish creek–Vallecito Basin, southern California. *Tectonics*, 31, TC2006. <https://doi.org/10.1029/2011TC003009>
- Elders, W. A., Rex, R. W., Robinson, P. T., Biehler, S., & Meidav, T. (1972). Crustal spreading in Southern California: The Imperial Valley and the Gulf of California formed by the rifting apart of a continental plate. *Science*, 178(4056), 15–24.
- Field, E. H., Biasi, G. P., Bird, P., Dawson, T. E., Felzer, K. R., Jackson, D. D., et al. (2013). Uniform California earthquake rupture forecast, version 3 (UCERF3)—The time-independent model: U.S. Geological Survey Open-File Report 2013–1165, 97 p., California Geological Survey Special Report 228, and Southern California Earthquake Center Publication 1792. [Available at <http://pubs.usgs.gov/of/2013/1165/>]
- Fletcher, J. M., & Spelz, R. M. (2009). Patterns of Quaternary deformation and rupture propagation associated with an active low-angle normal fault, Laguna Salada, Mexico: Evidence of a rolling hinge? *Geosphere*, 5(4), 385–407. <https://doi.org/10.1130/GES00206.1>
- Fletcher, J. M., Teran, O. J., Rockwell, T. K., Oskin, M. E., Hudnut, K. W., Mueller, K. J., et al. (2014). Assembly of a large earthquake from a complex fault system: Surface rupture kinematics of the 4 April 2010 El Mayor–Cucapah (Mexico) M_w 7.2 earthquake. *Geosphere*, 10(4), 797–827. <https://doi.org/10.1130/GES00933.1>
- Fletcher, K. E., Rockwell, T. K., & Sharp, W. D. (2011). Late Quaternary slip rate of the southern Elsinore fault, Southern California: Dating offset alluvial fans via $^{230}\text{Th}/\text{U}$ on pedogenic carbonate. *Journal of Geophysical Research*, 116, F02006. <https://doi.org/10.1029/2010JF001701>
- Hanks, T. C., & Kanamori, H. (1979). A moment magnitude scale. *Journal of Geophysical Research*, 84(B5), 2348–2350. <https://doi.org/10.1029/JB084iB05p02348>
- Hauksson, E., Stock, J., Hutton, K., Yang, W., Vidal-Villegas, J. A., & Kanamori, H. (2011). The 2010 M_w 7.2 El Mayor-Cucapah earthquake sequence, Baja California, Mexico and southernmost California, USA: Active seismotectonics along the Mexican Pacific margin. *Pure and Applied Geophysics*, 168(8–9), 1255–1277.
- Healy, D., Blenkinsop, T. G., Timms, N. E., Meredith, P. G., Mitchell, T. M., & Cooke, M. L. (2015). Polymodal faulting: Time for a new angle on shear failure. *Journal of Structural Geology*, 80, 51–71.
- Hill, D. P., Eaton, J. P., & Jones, L. M. (1990). Seismicity, 1980–86. In *The San Andreas Fault System, California*, USGS Prof. Paper 1515, (pp. 115–152). Washington, D. C.: U. S. GPO.
- Hough, S. E., & Elliot, A. (2004). Revisiting the 23 February 1892 Laguna Salada earthquake. *Bulletin of the Seismological Society of America*, 94(4), 1571–1578. <https://doi.org/10.1785/012003244>
- Huang, M. H., Fielding, E. J., Dickinson, H., Sun, J., Gonzalez-Ortega, J. A., Freed, A. M., & Bürgmann, R. (2017). Fault geometry inversion and slip distribution of the 2010 M_w 7.2 El Mayor-Cucapah earthquake from geodetic data. *Journal of Geophysical Research: Solid Earth*, 122, 607–621. <https://doi.org/10.1002/2016JB012858>
- Hudnut, K., Seeber, L., Rockwell, T., Goodmacher, J., Klinger, R., Lindvall, S., & McElwain, R. (1989). Surface ruptures on cross-faults in the 24 November 1987 Superstition Hills, California, earthquake sequence. *Bulletin of the Seismological Society of America*, 79, 330–341.

- Irwin, W. P. (1990). Geology and plate-tectonic development. In R. E. Wallace (Ed.), *The San Andreas Fault System, California, USGS Prof. Paper*, (Vol. 1515, pp. 61–80).
- Isaac, S. (1987). Geology and structure of the Yuha Desert between Ocotillo, California, USA and Laguna Salada, Baja California, Mexico (Doctoral dissertation, San Diego State University, Department of Geological Sciences).
- Jet Propulsion Laboratory (2018). GPS timeseries [Available at <http://sideshow.jpl.nasa.gov/post/series.html>]
- Kroll, K. A., Cochran, E. S., Richards-Dinger, K. B., & Sumy, D. F. (2013). Aftershocks of the 2010 M_w 7.2 El Mayor-Cucapah earthquake reveal complex faulting in the Yuha Desert, California. *Journal of Geophysical Research: Solid Earth*, 118, 6146–6164. <https://doi.org/10.1002/2013JB010529>
- Kroll, K. A., Richards-Dinger, K. B., Dieterich, J. H., & Cochran, E. S. (2017). Delayed seismicity rate changes controlled by static stress transfer. *Journal of Geophysical Research: Solid Earth*, 122, 7951–7965. <https://doi.org/10.1002/2017JB014227>
- Kyriakopoulos, C., Oglesby, D. D., Funning, G. J., & Ryan, K. J. (2017). Dynamic rupture modeling of the M7. 2 2010 El Mayor-Cucapah earthquake: Comparison with a geodetic model. *Journal of Geophysical Research: Solid Earth*, 122, 10,263–10,279. <https://doi.org/10.1002/2017JB014294>
- Magistrale, H., & Rockwell, T. (1996). The central and southern Elsinore fault zone, Southern California. *Bulletin of the Seismological Society of America*, 86, 1793–1803.
- Marone, C., Raleigh, C. B., & Scholz, C. H. (1990). Frictional behavior and constitutive modeling of simulated fault gouge. *Journal of Geophysical Research*, 95(B5), 7007–7025.
- Marone, C. J., Scholtz, C. H., & Bilham, R. (1991). On the mechanics of earthquake afterslip. *Journal of Geophysical Research*, 96(B5), 8441–8452.
- Meade, B. J., & Hager, B. H. (2005). Block models of crustal motion in southern California constrained by GPS measurements. *Journal of Geophysical Research*, 110, B03403. <https://doi.org/10.1029/2004JB003209>
- Millman, D. E., & Rockwell, T. K. (1986). Neotectonics of the Elsinore fault zone in Temescal Valley, California. In P. Ehlig (Ed.), *Neotectonics and faulting in Southern California* (pp. 159–166). Boulder, CO: Geological Society of America.
- Molnar, P., & Dayem, K. E. (2010). Major intracontinental strike-slip faults and contrasts in lithospheric strength. *Geosphere*, 6(4), 444–467. <https://doi.org/10.1130/GES00519.1>
- Mueller, K. J., & Rockwell, T. K. (1995). Late quaternary activity of the Laguna Salada fault in northern Baja California, Mexico. *Geological Society of America Bulletin*, 107(1), 8–18. [https://doi.org/10.1130/0016-7606\(1995\)107<0008:LQAOTL>2.3.CO;2](https://doi.org/10.1130/0016-7606(1995)107<0008:LQAOTL>2.3.CO;2)
- Nicholson, C., Seeber, L., Williams, P., & Sykes, L. R. (1986). Seismic evidence for conjugate slip and block rotation within the San Andreas fault system, southern California. *Tectonics*, 5(4), 629–648.
- Oertel, G. (1965). The mechanism of faulting in clay experiments. *Tectonophysics*, 2(5), 343–393. [https://doi.org/10.1016/0040-1951\(65\)90032-6](https://doi.org/10.1016/0040-1951(65)90032-6)
- Parker, J., Glasscoe, M., Donnellan, A., Stough, T., Pierce, M., & Wang, J. (2017). Radar determination of fault slip and location in partially decorrelated images. *Pure and Applied Geophysics*, 174(6), 2295–2310.
- Pollitz, F. F., Bürgmann, R., & Thatcher, W. (2012). Illumination of rheological mantle heterogeneity by the M7.2 2010 El Mayor-Cucapah earthquake. *Geochemistry, Geophysics, Geosystems*, 13, Q06002. <https://doi.org/10.1029/2012GC004139>
- Rockwell, T. K., Klinger, R., & Goodmacher, J. (1990). Determination of slip rates and dating of earthquakes for the San Jacinto and Elsinore fault zones. In M. A. Kooser & R. E. Reynolds (Eds.), *Geology around the Margins of the eastern San Bernardino Mountains, Volume 1: Inland Geological Society, Redlands* (pp. 51–56).
- Ross, Z. E., Rollins, C., Cochran, E. S., Hauksson, E., Avouac, J. P., & Ben-Zion, Y. (2017). Aftershocks driven by afterslip and fluid pressure sweeping through a fault-fracture mesh. *Geophysical Research Letters*, 44, 8260–8267. <https://doi.org/10.1002/2017GL074634>
- Rundle, J. B., Donnellan, A., Grant Ludwig, L., Gong, G., Turcotte, D. L., & Luginbuhl, M. (2016). Nowcasting earthquakes. *Earth and Space Science*, 3, 480–486. <https://doi.org/10.1002/2016EA000185>
- Rundle, J. B., Luginbuhl, M., Giguere, A., & Turcotte, D. L. (2018). Natural time, nowcasting and the physics of earthquakes: Estimation of seismic risk to global megacities. *Pure and Applied Geophysics*, 175, 647. <https://doi.org/10.1007/s00024-017-1720-x>
- Rymer, M. J., Treiman, J. A., Kendrick, K. J., Linenkaemper, J. J., Weldon, R. J., Bilham, R., et al. (2011). Triggered surface slips in southern California associated with the 2010 El Mayor-Cucapah, Baja California, Mexico, earthquake USGS Open-File Report 2010–1333 (Tech. Rep.). Pasadena, CA: US Geological Survey.
- Savage, J. C., & Svarc, J. L. (2009). Postseismic relaxation following the 1992 M7. 3 Landers and 1999 M7. 1 Hector Mine earthquakes, southern California. *Journal of Geophysical Research*, 114, B01401. <https://doi.org/10.1029/2008JB005938>
- Scholz, C. H. (1998). Earthquakes and friction laws. *Nature*, 391(6662), 37
- Sieh, K. E., & Williams, P. L. (1990). Behavior of the southernmost San Andreas fault during the past 300 years. *Journal of Geophysical Research*, 95(B5), 6629–6645.
- Stein, R. S., Barka, A. A., & Dieterich, J. H. (1997). Progressive failure on the North Anatolian fault since 1939 by earthquake stress triggering. *Geophysical Journal International*, 128(3), 594–604.
- Thorup, K., Rockwell, T., Magistrale, H., & Vanghan, P. (1997). Paleoseismology of the central Elsinore fault in southern California: Preliminary results from three trench sites, [abstracts with programs]. *Geological Society of America*, 29, 69–70.
- Thorup, K. M. (1997). Paleoseismology of the central Elsinore fault in southern California: Results from three trench sites, Master's Thesis, San Diego State University, 94 pp.
- Toksöz, M. N., Shakal, A. F., & Michael, A. J. (1979). Space-time migration of earthquakes along the North Anatolian fault zone and seismic gaps. *Pure and Applied Geophysics*, 117(6), 1258–1270.
- Topozada, T. R., Branum, D. M., Reichle, M. S., & Hallstrom, C. L. (2002). San Andreas Fault Zone, California: $M \geq 5.5$ Earthquake history. *Bulletin of the Seismological Society of America*, 92(7), 2555–2601.
- Treiman, J. A. (2012). Faults of the Yuha Desert and the southeastern portion of the Elsinore Fault Zone Imperial County, California, California Geological Survey Fault Evaluation Report FER-254.
- Vaughan, P., & Rockwell, T. (1986). Alluvial stratigraphy and neotectonics of the Elsinore fault zone at Agua Tibia Mountain, Southern California. In P. Ehlig (Ed.), *Neotectonics and faulting in Southern California* (pp. 177–191). Boulder, CO: Geological Society of America.
- Vaughan, P. R., Thorup, K. M., & Rockwell, T. K. (1999). Paleoseismology of the Elsinore fault at Agua Tibia Mountain southern California. *Bulletin of the Seismological Society of America*, 89(6), 1447–1457.
- Wang, J., Pierce, M., Donnellan, A., & Parker, J. (2015). *Pure and Applied Geophysics*, 172(8), 2325–2332. <https://doi.org/10.1007/s00024-014-0941-5>
- Wei, S., Fielding, E., Leprince, S., Sladen, A., Avouac, J. P., Helmerberger, D., et al. (2011). Superficial simplicity of the 2010 El Mayor-Cucapah earthquake of Baja California in Mexico. *Nature Geoscience*, 4(9), 615–618. <https://doi.org/10.1038/ngeo1213>
- Working Group on California Earthquake Probabilities (WGCEP) (2008). The Uniform California Earthquake Rupture Forecast, Version 2 (UCERF 2).
- Zumberge, J. F., Heflin, M. B., Jefferson, D. C., Watkins, M. M., & Webb, F. H. (1997). Precise point positioning for the efficient and robust analysis of GPS data from large networks. *Journal of Geophysical Research*, 102(B3), 5005–5017. <https://doi.org/10.1029/96JB03860>